Robotics and Autonomous Systems 120 (2019) 103247

Contents lists available at ScienceDirect

Robotics and Autonomous Systems

journal homepage: www.elsevier.com/locate/robot

Modeling and control of inherently safe robots with variable stiffness links☆

Siyang Song [a], Xianpai Zeng [b], Yu She [c], Junmin Wang [a,*], Hai-Jun Su [b]

[a] Walker Department of Mechanical Engineering, The University of Texas at Austin, Austin, TX 78712, USA
[b] Department of Mechanical and Aerospace Engineering, Ohio State University, Columbus, OH 43210, USA
[c] Computer Science & Artificial Intelligence Laboratory, Massachusetts Institute of Technology, Cambridge, MA 02139, USA

HIGHLIGHTS

- Inherently safe robots with variable stiffness links.
- Modeling, control and trajectory planning.
- Experimental evaluation and comparison.

ARTICLE INFO

Article history:
Received 4 February 2019
Received in revised form 15 June 2019
Accepted 22 July 2019
Available online 26 July 2019

Keywords:
Variable stiffness link
Physical human–robot interaction
Robust control
Vibration suppression
Safe trajectory planning
Impact test

ABSTRACT

In this paper, the modeling, control design, and trajectory planning for inherently safe robots with variable stiffness links (VSL) are investigated. Firstly, a dynamic model of VSL robots is developed using the pseudo-rigid-body model (PRBM). Based on PRBM, a feedback-linearization based controller is proposed. Extended state observer and deflection feedback are designed to improve the robustness and vibration suppression. To keep the inherent safety, a safe trajectory planning problem is formulated and the safety criterion is converted to a velocity constraint. With constraints on the jerk, acceleration, and velocity, the trajectory-planning problem is formulated as a time-optimal problem. The analytical solution of this problem is derived by optimal control theory. Experiments show the performances of motion control and vibration suppression of the proposed controller. The impact test results indicate the potential of VSL robots for applications with physical human–robot interaction.

1. Introduction

In the past decade, the physical human–robot interaction (pHRI) has become a popular research topic in robotic society. Traditional industrial robots may not suitable for direct interaction with human workers in the same workspace. With safety features, corobots enable their collaborations with humans. The safety of pHRI between corobots and human operators is always important. The safety of pHRI can be achieved in different ways. Typically, an impact between a robot and a human can be divided into three phases: pre-impact phase, impact phase, and post-impact phase. For impact phase and post-impact phase, strategies like collision detection and reaction [1–3] can significantly reduce injury severity. However, it is worth mentioning that such active strategies for impact phase and post-impact phase cannot decrease the injury severity of the impact in some situations such as high speed and rigid impact [4]. To achieve inherent safety, only measures in the impact phase and post-impact phase are not enough. New mechanical designs and control approaches for the pre-impact phase are also needed to enhance safety. To address the pre-impact design problem, methods such as obstacle avoidance [5,6], mechanical design optimization [7,8] and variable stiffness concept [2,9–11] are proposed. Among those approaches, variable stiffness link (VSL) is a synthesis of software (control, planning) and hardware (mechanical design). By tuning the link stiffness, VSL can compromise safety and efficiency in a better way. A low-stiffness configuration allows a faster motion while the safety is ensured. A high-stiffness configuration attenuates the vibration thus improve the positioning performance. Compared with the robots with rigid links, robots with VSL can have a light-weight link design, which is safe and economical for collaborative robot applications [12]. In 2012, a variable stiffness link design based on granular jamming and membrane coupling was proposed in [13]. A pneumatic actuated VSL design is introduced in [14] and collision reaction and detection control strategies are introduced in [2]. A VSL robot design based on layer jamming is introduced in [15]. In [16], a VSL robot based on the pneumatic artificial muscles (PAM) is proposed.

☆ The work is supported by NSF Award # 1637656.
* Corresponding author.
E-mail addresses: sysong@utexas.edu (S. Song), JWang@austin.utexas.edu (J. Wang).

https://doi.org/10.1016/j.robot.2019.07.017
0921-8890/

However, the control design for safe VSL robots is quite a challenge due to its complicated dynamics and safety requirements. For safe robots with VSL, control objectives and their challenges can be summarized as follows.

(1) Tracking of the desired joint trajectory (uncertainties and disturbances).

(2) Vibration suppression (varying flexibility).

(3) Inherent safety (pre-impact, impact, and post-impact phase).

For conventional flexible robots, the tracking control and vibration suppression have been studied in the past decades. Methods such as the feedback linearization [17], singular perturbation [18], input shaping [19], disturbance observer [20] and extended state observer [21] have been proposed for robots with constant flexibility. In the existing work, discussions on the VSL robot are still focused on mechanical design [14,22]. Discussions on control of VSL robot are not comprehensive and many problems are still open. In [2,23], collision detection and reaction strategies in the impact phase and post-impact phase are introduced. In [16], a controller based on inverse kinematics is designed for a VSL robot. However, dynamic control problems such as disturbance rejection and vibration suppression are not discussed. To address some of the aforementioned practical challenges for VSL robots, we propose a robust tracking control design with vibration suppression in this paper. To fulfill the inherent safety, a safe trajectory is planned based on optimal control.

In this paper, a dynamics model of VSL robots is developed by the pseudo-rigid-body model (PRBM) [24,25]. By lumping stiffness and discretizing links, a lumped model can be obtained. Inspired by previous works on conventional flexible robots such as [17,21], we extend the feedback linearization to VSL robots. By feedback linearization, the motor hub angle can be decoupled, which makes the tracking control design easier. To improve the robustness in engineering practice, the linearization-based controller is further enhanced by using an extended state observer (ESO). A deflection feedback is designed based on the singular perturbation theory to achieve better vibration suppression.

For the inherent safety of the VSL robots, we propose a trajectory planning method based on optimal control theory. By converting the safety criterion such as human injury criterion (HIC) to velocity limit, the trajectory planning problem is transferred to a constrained time-optimal control problem with input constraints and state constraints [9]. Solutions to such constrained trajectory planning problems can be given numerically [26–30] and analytically [9,31–33]. These solutions successfully give the constrained trajectory but they can still be improved. Firstly, online calculations can be minimized. Numerical solvers usually require a large number of iterations. Some analytical solvers such as [32] and [33] need online calculations to react to unforeseen events or obstacles. For inherently safe robots, the online calculations can be simplified because the robot should be safe for any unexpected contact. Secondly, in works such as [9] and [31], second-order trajectories are planned (with continuous velocity). For flexible robots, the high-order trajectory is preferred because a smooth trajectory can cause less vibrations. In this paper, we give a closed-form solution to the rest-to-rest motion trajectory based on optimal control theory. A third-order trajectory (with continuous acceleration) is planned. The canonical profile can be determined by a set of necessary conditions related to the final position and constraints, and can be determined offline thus the online calculations are minimized.

The contributions of this paper are as follows. Firstly, the dynamics of the VSL robot is modeled with the PRBM. Based on the PRBM, a tracking controller is designed considering the varying stiffness, robustness, and vibration suppression. Secondly, an analytical solution of the third-order safe trajectory is given by the optimal control theory. The canonical profile can be distinguished by a set of necessary conditions related to the final position and constraints. Online calculations are thus reduced. Finally, the effectiveness of the pre-impact strategies (including the dynamic controller and safe trajectory planning) are validated by both motion experiments and impact tests.

The remaining of this paper is organized as follows. In Section 2, the concept of a VSL robot is briefly introduced. Dynamic modeling and stiffness analysis are presented in this section too. Based on the dynamic model of the VSL, control design and trajectory planning are proposed in Section 3. In Section 4, experimental results validate the effectiveness of the proposed design. Conclusions are presented in Section 5.

2. Variable stiffness link

2.1. Variable stiffness link concept

The jamming technique is employed in our design to generate a significant stiffness variation. The jamming structures have been explored in past research as a variable stiffness solution [34,35], and they usually consist of two major components: a soft and deformable air-tight volume that is connected to a vacuum source which can generate and regulate the vacuum pressure; and a friction medium, either a granular material or overlapped sheets of material. The technique is known as granular jamming when granular material is used as the friction medium, and layer jamming when sheets of material are used. The pressure difference between the atmospheric pressure and the air pressure in the air-tight volume acts on the exterior surface of the deformable air-tight volume and it presses the granules or sheets against each other. Thus, it can increase the friction between them. The jamming leads to limited relative motion between granules or sheets. Meanwhile, it causes structural stiffness to increase. The stiffness of jamming structures goes from low in the case of no pressure difference and high in the case of the largest possible pressure difference. A continuum of stiffness values between the two extremes can be achieved by varying the pressure difference [36]. Ideally, a robot with layer jamming or granular jamming can safely handle a delicate object when the stiffness is low, but it can also lift large loads when the stiffness is increased.

Our design features a set of parallel-guided beams covered by overlapped friction layers that encapsulated in a sealed polyurethane bag. The center beam has a very low stiffness due to the thin backbone structure. Friction layers lay on the flat surfaces of multiple T-shaped supports. These T-shaped supports are designed to augment the effect of friction by increasing its leverage but not to touch each other when the beam is deformed, thus retaining the beam's flexibility. Fig. 1 shows the design of our variable stiffness link. More details about this design can be found in [15].

2.2. Pseudo-rigid-body model (PRBM)

The pseudo-rigid-body model (PRBM) [37] is a method for analysis and design of compliant mechanisms with lumped stiffness and discretized links. It provides a simple way to efficiently and accurately analyze statics and kinematics of compliant mechanisms subjected to large and nonlinear deformations. The PRBM started with the kinetostatic analysis [38–40] and recently was applied in dynamics analysis as well [41,42]. For the parallel-guiding VSL robot, the flexibility of each side of the link is lumped to two torsional springs in PRBM [43]. For the parallel-guiding VSL robot, there are four torsional springs in total, two for each side of the link. The lumping process is illustrated in Fig. 2.

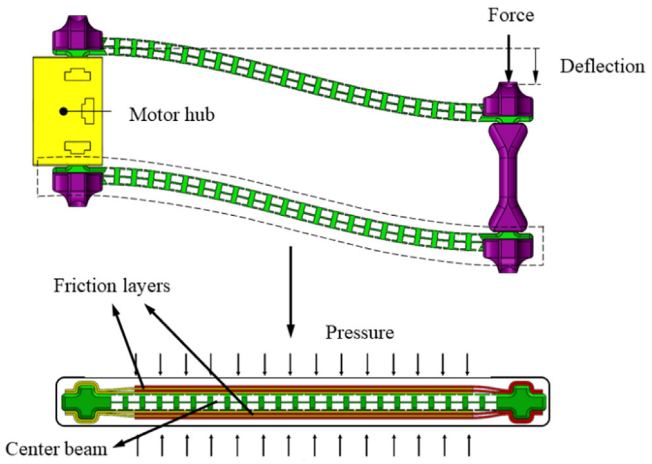

Fig. 1. Variable stiffness link design.

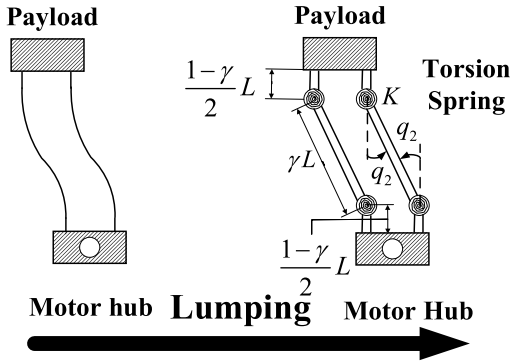

Fig. 2. Diagram of the PRBM.

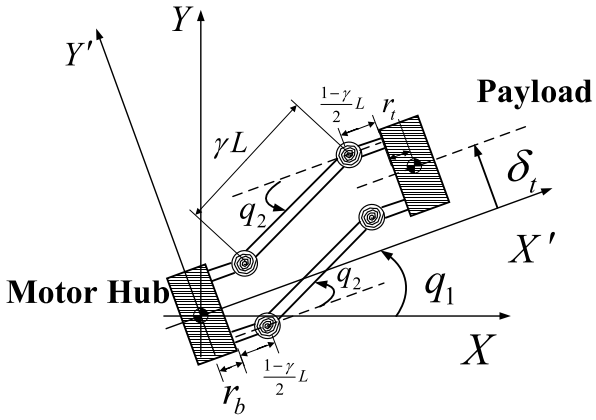

Fig. 3. Coordinate frames used in PRBM.

Note that the four torsional springs in PRBM are virtual joints. The torsional angle q_2 can be treated as a generalized coordinate of the vibration.

Each side of the link is separated into three rigid links with lengths of $(1-\gamma)L/2$, γL, and $(1-\gamma)L/2$ respectively, where L is the length of the link, γ is the characteristic radius of the PRBM.

Different from the constant stiffness link robots, the stiffness K can be tuned as needed. The lateral stiffness of the link K_L and the stiffness of torsional spring K have the following relationship

$$4 \cdot \frac{1}{2}Kq_2^2 = \frac{1}{2}K_L\delta_t^2 = \frac{1}{2}K_L(\gamma L \sin q_2)^2. \tag{1}$$

Under the small deflection assumption (q_2 is small), the stiffness of the torsional spring can be calculated by

$$K = \frac{1}{4}K_L\gamma^2 L^2. \tag{2}$$

More details about PRBM can be found in [41]. Based on the PRBM, we establish the dynamic model of the VSL robot.

The coordinate frames used for the modeling are illustrated in Fig. 3. In Fig. 3, q_1 is the motor angle, q_2 is the PRB joint torsional angle, δ_t is the tip deflection, (X, Y) is the global frame and (X', Y') is the local frame. The parallel-guiding arm has two different kinds of modal shapes. For the first kind of shapes, two sides of the link have the same motion/deformation in parallel. For the second kind of shapes, two sides of the link have symmetric motion/deformation. Considering the lateral load case, the second kind of shapes is neglected, and we assume the two sides of the link have the same motion/deformation. Therefore, only one variable is needed to represent the vibration, that is q_2. The dynamics model is established by the Euler–Lagrange equations. The first step is deriving the kinetic energy. Usually, the mass of the link is much smaller than the mass of payload and motor hub. To simplify the derivation, the masses of the first link and the third link are lumped to the inertia of the motor hub I_h and the mass of payload m_p, respectively. Then the velocity Jacobian of the two middle links can be derived as follows

$$J_{VL} = \begin{pmatrix} -(r_b + \frac{1-\gamma}{2}L)\sin q_1 - \frac{\gamma L}{2}\sin(q_1+q_2) & -\frac{\gamma L}{2}\sin(q_1+q_2) \\ (r_b + \frac{1-\gamma}{2}L)\cos q_1 + \frac{\gamma L}{2}\cos(q_1+q_2) & \frac{\gamma L}{2}\cos(q_1+q_2) \end{pmatrix}. \tag{3}$$

Similarly, the velocity Jacobian of the payload is as follows

$$J_{VP} = \begin{pmatrix} -(r_p + (1-\gamma)L)\sin q_1 - \gamma L \sin(q_1+q_2) & -\gamma L \sin(q_1+q_2) \\ (r_p + (1-\gamma)L)\cos q_1 + \gamma L \cos(q_1+q_2) & \gamma L \cos(q_1+q_2) \end{pmatrix}. \tag{4}$$

Let $\mathbf{q} = [q_1, q_2]^{\mathrm{T}}$. Then the translational kinetic energy T_1 is

$$T_1 = \frac{1}{2}\dot{\mathbf{q}}^T(2m_l J_{VL}^T(\mathbf{q})J_{VL}(\mathbf{q}) + m_p J_{VP}^T(\mathbf{q})J_{VP}(\mathbf{q}))\dot{\mathbf{q}}, \tag{5}$$

in which m_l is the mass of each side of the link, m_p is the mass of the payload. The rotational kinetic energy can be derived as follows

$$\begin{aligned} T_2 &= \frac{1}{2}I_h\dot{q}_1^2 + \frac{1}{2}I_p\dot{q}_1^2 + 2\cdot\frac{1}{2}I_L(\dot{q}_1+\dot{q}_2)^2 \\ &= \frac{1}{2}\dot{\mathbf{q}}^{\mathrm{T}}\begin{pmatrix} I_h + I_p + 2I_L & 2I_L \\ 2I_L & 2I_L \end{pmatrix}\dot{\mathbf{q}}, \end{aligned} \tag{6}$$

where I_h is the inertia of the motor hub, I_p is the inertia of the payload, and I_L is the inertia of each side of the link. Then, we can obtain the total kinetic energy as follows

$$T = T_1 + T_2 = \frac{1}{2}\dot{\mathbf{q}}^T M(\mathbf{q})\dot{\mathbf{q}}, \tag{7}$$

where

$$\begin{aligned} M(\mathbf{q}) = {} & 2m_l J_{VL}^T(\mathbf{q})J_{VL}(\mathbf{q}) + m_p J_{VP}^T(\mathbf{q})J_{VP}(\mathbf{q}) \\ & + \begin{pmatrix} I_h + I_p + 2I_L & 2I_L \\ 2I_L & 2I_L \end{pmatrix}. \end{aligned} \tag{8}$$

The matrix $M(\mathbf{q})$ is the inertia matrix. The potential energy contains the elastic energy of the four torsion springs.

$$U(\mathbf{q}) = 4 \cdot \frac{1}{2} K q_2^2. \tag{9}$$

Then we can derive the Euler–Lagrange equations by define

$$L = T - U, \tag{10}$$

and

$$\frac{d}{dt}\frac{\partial L}{\partial \dot{q}_k} - \frac{\partial L}{\partial q_k} = u_k, k = 1, 2. \tag{11}$$

To facilitate the analysis, we introduce the Christoffel symbols [44]

$$c_{ijk} = \frac{1}{2}\left\{\frac{\partial m_{kj}}{\partial q_i} + \frac{\partial m_{ki}}{\partial q_j} - \frac{\partial m_{ij}}{\partial q_k}\right\}, \tag{12}$$

where m_{ij} is the (i, j)th element of the inertia matrix $M(\mathbf{q})$. Then we can obtain the Euler–Lagrange equations as

$$M(\mathbf{q})\ddot{\mathbf{q}} + \sum_{i,j} c_{ijk}\dot{q}_i\dot{q}_j + \phi(\mathbf{q}) = \boldsymbol{\tau}, \tag{13}$$

where

$$\phi(\mathbf{q}) = -\frac{\partial L}{\partial \mathbf{q}} = \begin{pmatrix} 0 \\ 4Kq_2 \end{pmatrix}, \quad \boldsymbol{\tau} = \begin{pmatrix} \tau \\ 0 \end{pmatrix}, \tag{14}$$

in which τ is the input torque. The second term in (13) includes the Coriolis and the centrifugal terms. We can rewrite the second term with $\sum_{i,j} c_{ijk}\dot{q}_i\dot{q}_j = C(\mathbf{q}, \dot{\mathbf{q}})\dot{\mathbf{q}}$. The (k, j)th element of the matrix $C(\mathbf{q}, \dot{\mathbf{q}})$ can be derived from the Christoffel symbols as follows

$$c_{kj} = \sum_{i=1}^{2} c_{ijk}(\mathbf{q})\dot{q}_i. \tag{15}$$

Rewrite the Euler–Lagrange equations, and we have the dynamics of the VSL robots as follows

$$M(\mathbf{q})\ddot{\mathbf{q}} + C(\mathbf{q}, \dot{\mathbf{q}})\dot{\mathbf{q}} + \begin{pmatrix} 0 \\ 4Kq_2 \end{pmatrix} = \begin{pmatrix} \tau \\ 0 \end{pmatrix}. \tag{16}$$

Remark 1. Due to the mechanical constraints, the four torsional springs have the same torsion with the angle q_2. Thus, the degrees of freedom of the robot is two.

Remark 2. The feedback of the torsion angle q_2 can be estimated by the tip deflection. Assume that q_2 is a small angle then we have

$$q_2 = \arctan\frac{\delta_t}{\gamma L} \approx \frac{\delta_t}{\gamma L}. \tag{17}$$

In the practice, the tip deflection is measured by strain gauges [45].

The inertia matrix has the following property that will be used in the control design.

Property 1. *$M(\mathbf{q})$ is positive definite and $M_{ij} > 0, \forall i, j$.*

2.3. Stiffness analysis

In our VSL concept, the stiffness is related to the pressure difference. In this process, different factors play different roles in stiffness variation. Material and friction play the two most critical roles in stiffness variation.

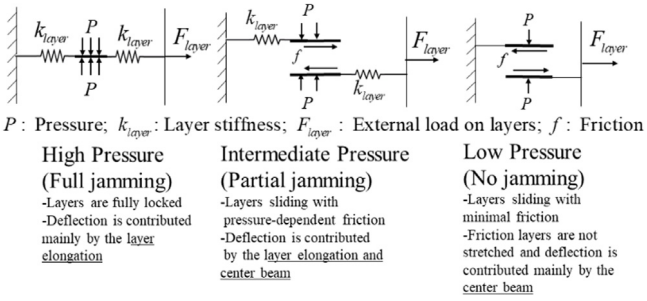

Fig. 4. Stiffness change mechanisms under different pressure.

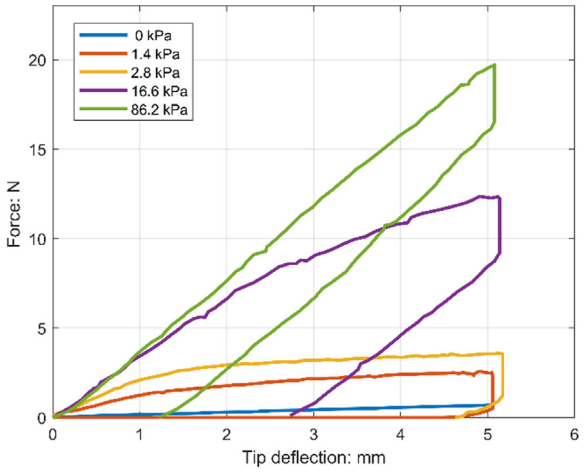

Fig. 5. Force vs. Tip deflection.

Fig. 4 illustrates the mechanisms of stiffness change under different pressure. In low-pressure case, no jamming happens, and the center beam can deflect easily due to the small frictions between the layers. With the increase of the pressure, the frictions between layers increase and the more loads are transferred to the layers from the center beam. When full jamming happens, most loads are on the layers and the stiffness behavior depends on layer elongation. Note that in Fig. 4, these mechanisms are only valid for small deflections (typically smaller than 2 mm). When the deflection is large, the friction layers will slide, and the stiffness of the arm will be small like the low-pressure case. This phenomenon can be observed in the stiffness test. Fig. 5 shows the result of the stiffness test. Note that for the low-pressure case (such as 1.4 kPa and 2.8 kPa in Fig. 5), the sliding between friction layers happens easily. After the layers start sliding, the stiffness of the arm will become small. When the deflection is small, layer sliding and layer elongation contribute to the stiffness simultaneously. In this paper, we ignore the large deflection case and assume the stiffness is a constant when the deflection is small (deflection is less than 2 mm). The participation of layer elongation and sliding depends on the pressure difference.

From the discussion above we know that the stiffness of the link is related to the pressure. In this paper, the relationship between the pressure and the stiffness is fitted by the experimental results as the following function.

$$K_L = 264.3 + 2982.4\exp(2.87\text{E}-6p) - 3081.2\exp(-2.85\text{E}-4p). \tag{18}$$

The unit of the pressure p and the stiffness of the link K_L are Pa and N/m, respectively. Fig. 6 shows the fitting of the stiffness model.

By using this stiffness model, the stiffness can be controlled by regulating the pressure difference.

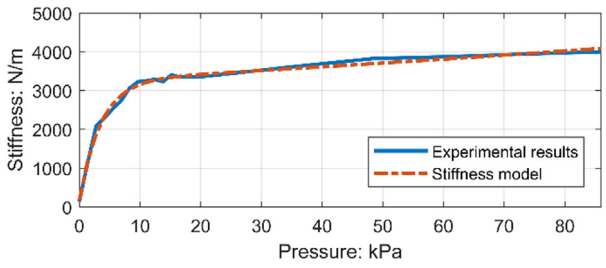

Fig. 6. Stiffness test results and stiffness model.

3. Control design and trajectory planning

In this section, the input–output feedback linearization (FL) based controller is introduced first. Based on this controller, improvements including the extended state observer and deflection feedback are augmented to address the concerns on robustness and vibration. After that, the safe trajectory planning problem is formulated and the analytical solution to the problem is given.

3.1. Input–Output Feedback Linearization

The feedback linearization is a popular technique for control design of robots. It can decouple the system variables either partially or globally. By linearizing the system, linear control law can be implemented on the decoupled system. Literature has shown that rigid robots and flexible joint robots can be globally linearized [21,44]. The situation of VSL robots is different. In this section, we will use input–output feedback linearization to design a tracking controller for VSL robots. Recall the dynamic equations of the VSL robots (16). To facilitate the analysis, let

$$M(\mathbf{q}) = \begin{pmatrix} M_{11} & M_{12} \\ M_{21} & M_{22} \end{pmatrix}, C(\mathbf{q}, \dot{\mathbf{q}}) = \begin{pmatrix} C_{11} & C_{12} \\ C_{21} & C_{22} \end{pmatrix}. \tag{19}$$

Note that $C_{22} = 0$ then the dynamics can be rewritten as

$$M_{11}\ddot{q}_1 + M_{12}\ddot{q}_2 + C_{11}\dot{q}_1 + C_{12}\dot{q}_2 = \tau, \tag{20}$$

$$M_{21}\ddot{q}_1 + M_{22}\ddot{q}_2 + C_{21}\dot{q}_1 + 4Kq_2 = 0. \tag{21}$$

First, we choose the motor angle q_1 as the output. To solve the q_1 dynamics, solve $\ddot{q}_2$ from (21) first. That is

$$\ddot{q}_2 = -M_{22}^{-1}(M_{21}\ddot{q}_1 + C_{21}\dot{q}_1 + 4Kq_2). \tag{22}$$

Substitute (22) into (20), we can obtain

$$\begin{aligned} &\overline{M}\ddot{q}_1 + \overline{C}_1\dot{q}_1 + \overline{C}_2\dot{q}_2 + \overline{K} = \tau, \\ &\overline{M} = M_{11} - M_{12}M_{22}^{-1}M_{21}, \\ &\overline{C}_1 = C_{11} - M_{12}M_{22}^{-1}C_{21}, \\ &\overline{C}_2 = C_{12}, \\ &\overline{K} = -4M_{12}M_{22}^{-1}Kq_2. \end{aligned} \tag{23}$$

If we choose the torque as follows

$$\tau = \overline{M}v + \overline{C}_1\dot{q}_1 + \overline{C}_2\dot{q}_2 + \overline{K}, \tag{24}$$

where v is the control to be designed. Now (20) is linearized as

$$\ddot{q}_1 = v. \tag{25}$$

A typical choice for the control v is the proportional–derivative (PD) control

$$v = \ddot{q}_d - K_P(q_1 - q_d) - K_D(\dot{q}_1 - \dot{q}_d), \tag{26}$$

in which q_d is the desired joint trajectory. Then the dynamics of the tracking error $e = q_1 - q_d$ is governed by the following equation

$$(\ddot{q}_1 - \ddot{q}_d) + K_D(\dot{q}_1 - \dot{q}_d) + K_P(q_1 - q_d) = 0. \tag{27}$$

The tracking error will converge to zero asymptotically if we choose $K_P > 0, K_D > 0$. Now, the closed-loop system can be rewritten as

$$\begin{aligned} &\ddot{q}_1 = v, \\ &\ddot{q}_2 = -M_{22}^{-1}(M_{21}\ddot{q}_1 + C_{21}\dot{q}_1 + 4Kq_2), \end{aligned} \tag{28}$$

where the second equation in (28) describes the internal dynamics. By letting the output $q_1 = \dot{q}_1 = \ddot{q}_1 = 0$, the zero dynamics can be derived from the internal dynamics, that is

$$\ddot{q}_2 = -4M_{22}^{-1}Kq_2. \tag{29}$$

From Property 1, we know $M_{22} > 0$. On the other hand, varying stiffness K is also greater than zero. Therefore the zero dynamics is critically stable. In practice, flexible links usually have internal damping such as viscous friction. With the damping term, the zero dynamics (29) can be asymptotically stable. Then the origin of the closed-loop system (28) is asymptotically stable by Lemma 13.1 in [46].

Though the analysis shows that the above design has achieved the tracking of the trajectory, some issues may arise during practice. First, the feedback linearization procedure (24) needs accurate model information such as mass, payload, and dimensions. However, it is common that some parameters may be inaccurate or even unknown in practice. Besides, the mechanical transmissions such as the motor and gearbox may introduce unexpected disturbances, such as friction. With the uncertainties and disturbances mentioned above, the robustness and the performance of the closed-loop system may be attenuated. In the next section, we will introduce the implementation of the extended state observer to address the robustness problem.

3.2. Extended state observer

To deal with the robustness problem in the feedback linearization, we propose to use the extended state observer (ESO) to deal with the uncertainties and disturbances. Let the nominal model of the robots be

$$\widehat{M}_{11}\ddot{q}_1 + \widehat{M}_{12}\ddot{q}_2 + \widehat{C}_{11}\dot{q}_1 + \widehat{C}_{12}\dot{q}_2 = \tau + f_{ext} + f_u, \tag{30}$$

$$\widehat{M}_{21}\ddot{q}_1 + \widehat{M}_{22}\ddot{q}_2 + \widehat{C}_{21}\dot{q}_1 + 4\widehat{K}q_2 = 0, \tag{31}$$

where the parameter with the hat is the nominal value of the corresponding parameter, f_{ext} is the external disturbance such as the friction and f_u is the unmodeled dynamics. Then the nominal feedback linearization law will be

$$\tau = \widehat{\overline{M}}v + \widehat{\overline{C}}_1\dot{q}_1 + \widehat{\overline{C}}_2\dot{q}_2 + \widehat{\overline{K}}, \tag{32}$$

and

$$\begin{aligned} &\widehat{\overline{M}} = \widehat{M}_{11} - \widehat{M}_{12}\widehat{M}_{22}^{-1}\widehat{M}_{21}, \\ &\widehat{\overline{C}}_1 = \widehat{C}_{11} - \widehat{M}_{12}\widehat{M}_{22}^{-1}\widehat{C}_{21}, \\ &\widehat{\overline{C}}_2 = \widehat{C}_{12}, \\ &\widehat{\overline{K}} = -4\widehat{M}_{12}\widehat{M}_{22}^{-1}\widehat{K}q_2. \end{aligned} \tag{33}$$

The dynamics after the linearization will be

$$\begin{aligned} &\overline{M}\ddot{q}_1 + \overline{C}_1\dot{q}_1 + \overline{C}_2\dot{q}_2 + \overline{K} \\ &= \widehat{\overline{M}}v + \widehat{\overline{C}}_1\dot{q}_1 + \widehat{\overline{C}}_2\dot{q}_2 + \widehat{\overline{K}} + f_{ext} + f_u. \end{aligned} \tag{34}$$

Let

$$\begin{aligned}\widehat{\overline{M}} &= \overline{M} + \delta\overline{M},\\ \widehat{\overline{C}}_1 &= \overline{C}_1 + \delta\overline{C}_1,\\ \widehat{\overline{C}}_2 &= \overline{C}_2 + \delta\overline{C}_2,\\ \widehat{\overline{K}} &= \overline{K} + \delta\overline{K},\end{aligned} \tag{35}$$

where δ denotes the uncertainty. Rewrite (34) we can obtain

$$\overline{M}\ddot{q}_1 = \overline{M}v + \delta\overline{M}v + \delta\overline{C}_1\dot{q}_1 + \delta\overline{C}_2\dot{q}_2 + \delta\overline{K} + f_{ext} + f_u. \tag{36}$$

Furthermore, we have

$$\ddot{q}_1 = v + \overline{M}^{-1}(\delta\overline{M}v + \delta\overline{C}_1\dot{q}_1 + \delta\overline{C}_2\dot{q}_2 + \delta\overline{K} + f_{ext} + f_u). \tag{37}$$

We use d to represent the generalized disturbance. Rewrite (37)

$$\begin{aligned}\ddot{q}_1 &= v + d,\\ d &= \overline{M}^{-1}(\delta\overline{M}v + \delta\overline{C}_1\dot{q}_1 + \delta\overline{C}_2\dot{q}_2 + \delta\overline{K} + f_{ext} + f_u).\end{aligned} \tag{38}$$

To employ the ESO, first, we need to extend the generalized disturbance d in (20) to a new system state. Let $\mathbf{x} = [q_1, \dot{q}_1, d]^{\mathrm{T}}$, (38) can be rewritten as

$$\begin{aligned}\dot{x}_1 &= x_2,\\ \dot{x}_2 &= x_3 + v,\\ \dot{x}_3 &= h(\mathbf{x}, t),\end{aligned} \tag{39}$$

where $h(\mathbf{x}, t)$ is the derivative of the generalized disturbance. Here we have a standard assumption for d and $h(\mathbf{x}, t)$.

Assumption 1 ([47]). The generalized disturbance d is bounded and differentiable. Its derivative $h(\mathbf{x}, t)$ is bounded.

For convenience, we write (39) in a state-space form

$$\begin{aligned}\dot{x} &= Ax + Bv + Eh,\\ A = \begin{pmatrix}0 & 1 & 0\\ 0 & 0 & 1\\ 0 & 0 & 0\end{pmatrix}, B &= \begin{pmatrix}0\\ 1\\ 0\end{pmatrix}, E = \begin{pmatrix}0\\ 0\\ 1\end{pmatrix}.\end{aligned} \tag{40}$$

To estimate the generalized disturbance, we design a linear ESO (LESO) for system (40)

$$\dot{\hat{x}} = A\hat{x} + Bv + LC(x - \hat{x}), \tag{41}$$

where $L = [\beta_1 \quad \beta_2 \quad \beta_3], \beta_i > 0, i = 1, 2, 3$ is the observer gain vector and $C = [1 \quad 0 \quad 0]$. The stability of LESO is given in Theorem 1 in [47]. For an unknown but bounded $h(\mathbf{x}, t)$, the observer error $e_o = x - \hat{x}$ will convergent to a neighbor of the origin in finite time.

Now, the generalized disturbance d can be estimated by the observer state $\hat{x}_3$. Combined with the PD control law (26), the new control law will be

$$v = \ddot{q}_d - K_P(q_1 - q_d) - K_D(\dot{q}_1 - \dot{q}_d) - \hat{x}_3. \tag{42}$$

Define the tracking error $e_t = [x_1 - q_d \quad \dot{x}_1 - \dot{q}_d]^{\mathrm{T}}$, and then the closed-loop system with control law (42) can be written as follows

$$\begin{pmatrix}\dot{e}_c\\ \dot{e}_o\end{pmatrix} = \begin{pmatrix}A_c & B_cC_c\\ 0 & A - LC\end{pmatrix}\begin{pmatrix}e_c\\ e_o\end{pmatrix} + \begin{pmatrix}0\\ E\end{pmatrix}h, \tag{43}$$

with

$$A_c = \begin{pmatrix}0 & 1\\ -K_P & -K_D\end{pmatrix}, B_c = \begin{pmatrix}0\\ 1\end{pmatrix}, C_c = \begin{pmatrix}0 & 0 & 1\end{pmatrix}. \tag{44}$$

It is clear that the internal stability of the system (43) can be guaranteed by choosing K_P, K_D, L appropriately. Furthermore, because $h(\mathbf{x}, t)$ is bounded, the bounded input-bounded output stability (BIBO) can be inferred. The analysis of the zero dynamics remains the same as (29).

Note that the estimation error of ESO does not converge to zero asymptotically. Therefore, the estimation errors may have some fluctuations around zero at steady state, especially when the gain of ESO is small. If the gain is too large, the convergence of the estimation error at the beginning may have significant overshoot. These two features may excite undesired vibrations of the link, especially when the gain of the ESO is not proper (too small or too large). To address the vibration suppression, we propose a deflection feedback design based on the singular perturbation theory.

3.3. Deflection feedback

The feedback linearization and the ESO have addressed the robustness problem but the vibration suppression is not considered. In this section, a deflection feedback mechanism is designed to overcome this drawback. Compared with the motion of the motor angle q_1, the vibration is a relatively fast varying variable. In this paper, we treat the PRB joint torsional angle q_2 as the fast variable and we will design deflection feedback based on the singular perturbation theory. First, we rewrite the system dynamics into the standard form of the singular perturbation problem. Consider the system (38) and the internal dynamics

$$\ddot{q}_2 = -M_{22}^{-1}(M_{21}\ddot{q}_1 + C_{21}\dot{q}_1 + 4Kq_2). \tag{45}$$

Choose

$$\varepsilon = \frac{1}{4M_{22}^{-1}K} > 0. \tag{46}$$

Note that the parameter ε in the singular perturbation problem is usually small. In our case, M_{22} is usually a small constant. This property ensures that the parameter ε is small enough. Let $\varepsilon\mathbf{z} = \varepsilon \cdot [z_1, z_2]^{\mathrm{T}} = [q_2, \dot{q}_2]^{\mathrm{T}}$ then we can obtain the standard singular perturbation problem from (45) and (38).

$$\ddot{q}_1 = v + d, \tag{47}$$

$$\begin{aligned}\varepsilon\dot{z}_2 &= -M_{22}^{-1}(M_{21}v + C_{21}\dot{q}_1) - 4M_{22}^{-1}K\varepsilon z_1\\ &= -M_{22}^{-1}(M_{21}v + C_{21}\dot{q}_1) - z_1.\end{aligned} \tag{48}$$

Now, define the control with deflection feedback as

$$v = \overline{v} + u_s, \tag{49}$$

where u_s is the fast component of control and $\overline{v}$ is the slow component of control (42). We will discuss the design of u_s later. Let $\varepsilon = 0$ and $u_s = 0$, (47) and (48) will degenerate to (48)

$$\ddot{\overline{q}}_1 = \overline{v} + d, \tag{50}$$

$$0 = -M_{22}^{-1}(M_{21}\overline{v} + C_{21}\dot{q}_1) - \overline{z}_1, \tag{51}$$

and we can solve $\overline{z}_1$ from (51), that is

$$\overline{z}_1 = h_s(\overline{q}_1, \dot{\overline{q}}_1) = -M_{22}^{-1}(M_{21}\overline{v} + C_{21}\dot{q}_1). \tag{52}$$

Let $\tau_s = t/\varepsilon$ and $y_1 = z_1 - \overline{z}_1, y_2 = \varepsilon z_2$, we can obtain the following equations by substituting τ_s and y into the problem (47) and (48)

$$\begin{aligned}\frac{dy_1}{d\tau_s} &= y_2 - \varepsilon\frac{\partial h_s}{\partial t},\\ \frac{dy_2}{d\tau_s} &= \frac{dy_2}{dt}\frac{dt}{d\tau_s} = -M_{22}^{-1}(M_{21}v + C_{21}\dot{q}_1) - (y_1 + \overline{z}_1).\end{aligned} \tag{53}$$

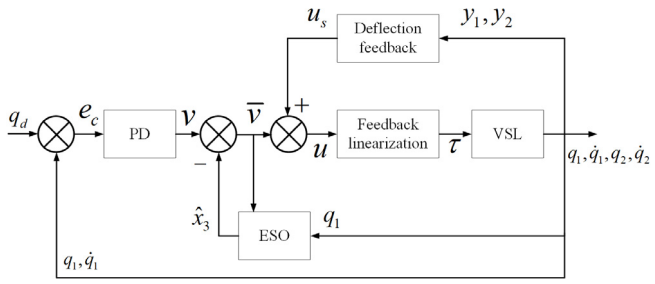

Fig. 7. Diagram of the controller.

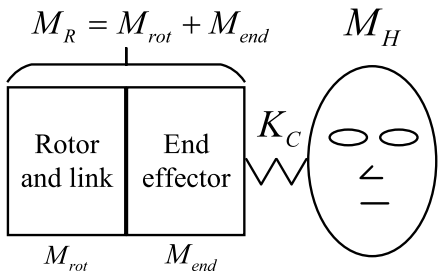

Fig. 8. Mass–spring–mass impact model (Traditional robot)

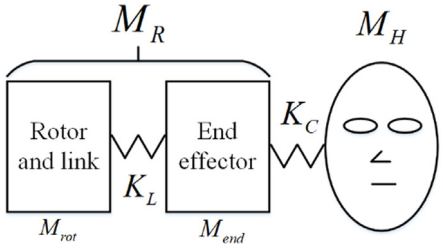

Fig. 9. Mass–spring–mass impact model (VSL)

Set $\varepsilon = 0$ for (53), we can obtain the boundary-layer model

$$\begin{aligned}\frac{dy_1}{d\tau_s} &= y_2,\\ \frac{dy_2}{d\tau_s} &= -M_{22}^{-1}(M_{21}v + C_{21}\dot{q}_1) - (y_1 + \bar{z}_1)\\ &= -M_{22}^{-1}(M_{21}v + C_{21}\dot{q}_1)\\ &\quad -(y_1 - M_{22}^{-1}(M_{21}\bar{v} + C_{21}\dot{q}_1))\\ &= -M_{22}^{-1}M_{21}u_s - y_1.\end{aligned} \tag{54}$$

Choose the deflection feedback u_s as

$$u_s = M_{22}M_{21}^{-1}(\alpha_1 y_1 + \alpha_2 y_2), \tag{55}$$

the boundary-layer model (54) will then be

$$\begin{aligned}\frac{dy_1}{d\tau_s} &= y_2,\\ \frac{dy_2}{d\tau_s} &= -(\alpha_1 + 1)y_1 - \alpha_2 y_2.\end{aligned} \tag{56}$$

It is straightforward to select $\alpha_1 + 1 > 0, \alpha_2 > 0$ to ensure the origin of (56) is exponentially stable. By the Tikhonov theorem (Theorem 11.1 in [46]), the following relationship holds

$$\begin{aligned}q_1(t,\varepsilon) - \bar{q}_1(t,\varepsilon) &= O(\varepsilon),\\ y(t,\varepsilon) - \hat{y}(t,\varepsilon) &= O(\varepsilon),\end{aligned} \tag{57}$$

where $\bar{q}_1(t,\varepsilon)$ is the solution of the slow system (50) and the $\hat{y}(t,\varepsilon)$ is the solution of the boundary-layer model (56). By tuning parameters α_i, the behavior of $\hat{y}(t,\varepsilon)$ can be governed by the desired convergence rate. Furthermore, $y(t,\varepsilon)$ and $\hat{y}(t,\varepsilon)$ have similar asymptotic behaviors, which makes the suppression of vibration more efficiently. The feedback y_1, y_2 can be calculated with the relationship $y_1 = z_1 - \bar{z}_1 = q_2/\varepsilon - h_s(\bar{q}_1, \dot{\bar{q}}_1), y_2 = \varepsilon z_2 = \dot{q}_2$. Because q_2 can be obtained from the deflection, we call the feedback y_1, y_2 the deflection feedback.

For the control law (49), if we choose $\bar{v}$ from (42) and u_s from (55), the controller will have good robustness and the performance on vibration suppression will be improved as well. The full diagram of the controller is shown in Fig. 7.

3.4. Trajectory planning

3.4.1. Head injury criterion (HIC)

During the execution of the task, a safe trajectory is needed. Different safety criteria were developed to evaluate the safety level. Popular criteria such as the Head Injury Criterion (HIC) [48] and maximum impact force [49] have been applied to robotics. To evaluate the safety level of the trajectory, HIC is used in this paper.

The definition of HIC [48,50] is as follows

$$HIC(\Delta t_{\max}) = \max_{t_1,t_2}[(\frac{1}{t_2 - t_1}\int_{t_1}^{t_2} \hat{a}\, dt)^{2.5}(t_2 - t_1)], \tag{58}$$

subject to $t_2 - t_1 \le \Delta t_{\max}$.

In which, $\hat{a} = a/g$ is the head acceleration normalized by the acceleration of gravity ($g = 9.8$ m/s^2). $\Delta t_{max} = 15$ ms is the maximum time interval.

To obtain the analytical solution of HIC, a mass–spring–mass model is introduced. The model is illustrated in Fig. 8.

In Fig. 8, M_{rot} and M_{end} are coupled together and the effective mass of the robot during the impact is $M_R = M_{rot} + M_{end}$. M_H is the mass of the head. K_C is the contact stiffness between robot and head (not the stiffness of the robot). Based on the mass–spring–mass model, an analytical solution of HIC is given in [48]

$$HIC_{15} = 0.00433(\frac{K_C}{M_H})^{3/4}(\frac{M_R}{M_H + M_R})^{7/4}v^{5/2}, \tag{59}$$

where v is the relative velocity between the robot and head.

For robots with VSL, the situation is different because M_{rot} and M_{end} are decoupled with changing of the link stiffness. Fig. 9 shows the impact model of the robot with VSL.

The decoupling of M_{rot} and M_{end} during the impact depends on the variation of the link stiffness K_L. When the decoupling happens, the effective mass M_R is reduced. This relationship can be described by the following Eq. [31]

$$M_R(K_L) = M_{end} + \frac{K_L}{K_L + \eta}M_{rot}. \tag{60}$$

Note that the effective mass during the impact is an equivalent mass to describe the mass decoupling. The total mass of the robot is not physically changed. Mechanical design of the VSL such as mass (M_{end} and M_{rot}) and the stiffness (K_L) can affect the decoupling. Interested reader can refer to [12]. When K_L is large (stiff link), M_R is close to $M_{end} + M_{rot}$. When K_L is small (soft link), $M_R \approx M_{end} + M_{rot}/\eta$. Usually, the constant η is a large number. Substituting (60) into (59) then we have

$$HIC_{15} = 0.00433(\frac{K_C}{M_H})^{3/4}(\frac{M_R(K_L)}{M_H + M_R(K_L)})^{7/4}v^{5/2}. \tag{61}$$

Based on (60), softer robots decouple more mass during the impact and thus allow faster and safe motions. For a given permissible HIC_{max} and the smallest link stiffness K_{min}, the maximum

speed v_{max} can be determined by

$$v_{max}(HIC_{\max}, K_{\min}) = \left(\frac{HIC_{max}}{0.00433(\frac{K_C}{M_H})^{3/4}(\frac{M_R(K_{min})}{M_H+M_R(K_{min})})^{7/4}} \right)^{2/5}. \quad (62)$$

The selection of HIC_{max} may affect the potential injury level of human operators and readers can refer to [4,51] about more details.

3.4.2. Optimal trajectory planning

With given permissible HIC_{max}, velocity limit VC can be calculated from v_{max}. Limits on actuators (motor torque, stiffness actuator) can be converted to acceleration limit AC in practice. To attenuate vibrations of the flexible link, the jerk limit JC is also considered in trajectory planning. With those kinematic constraints, a time-optimal trajectory planning problem for the rest-to-rest task can be formulated as (63).

$$\min \int_0^T 1\mathrm{dt} \ \text{subject to:} \quad \begin{cases} q_1(0) = 0, q_1(T) = q_d \\ \dot{q}_1(0) = 0, \dot{q}_1(T) = 0 \\ \ddot{q}_1(0) = 0, \ddot{q}_1(T) = 0 \end{cases} \text{and} \quad \begin{cases} |\dot{q}_1| \le VC \\ |\ddot{q}_1| \le AC \\ |\dddot{q}_1| \le JC \end{cases}, \quad (63)$$

where the first column in (63) are the initial and terminal conditions. q_d is the desired position. VC, AC and JC are velocity limit, acceleration limit, and jerk limit, respectively. The time-optimal problem (63) is an optimal control problem with state variable inequality constraints (SVIC). Here, VC and AC are state constraints and JC is input constraint. Analytical solutions to such problems are difficult to solve because of constraints. First, we will show the solution to this problem is a bang–bang control. Second, with a bang–bang control, solutions in different situations are given.

To facilitate the analysis, state constraints are rewritten as follows

$$\begin{cases} VC - \dot{q}_1 \ge 0 \\ \dot{q}_1 + VC \ge 0 \\ AC - \ddot{q}_1 \ge 0 \\ \ddot{q}_1 + AC \ge 0 \end{cases}. \quad (64)$$

Define $[x_1, x_2, x_3] = [q_1, \dot{q}_1, \ddot{q}_1]$ and $u = \dddot{q}_1$. To handle the constraints, a new variable x_4 is introduced in here and it is defined by

$$\begin{aligned} \dot{x}_4 = {} & [H(\dot{q}_1 - VC)]^2 + [H(-\dot{q}_1 - VC)]^2 \\ & + [H(\ddot{q}_1 - AC)]^2 + [H(-\ddot{q}_1 - AC)]^2. \end{aligned} \quad (65)$$

The function $H(\cdot)$ is the Heaviside function defined by

$$H(-f) = \begin{cases} 0, \ \text{for} f \ge 0 \\ 1, \ \text{for} f < 0 \end{cases}. \quad (66)$$

The Hamiltonian of the system can be formed as follows

$$\begin{aligned} & \mathcal{H}(\mathbf{x}(t), u(t), \boldsymbol{\lambda}(t)) = 1 + \lambda_1 x_2 + \lambda_2 x_3 + \lambda_3 u \\ & + \lambda_4([H(\dot{q}_1 - VC)]^2 + [H(-\dot{q}_1 - VC)]^2 \\ & + [H(\ddot{q}_1 - AC)]^2 + [H(-\ddot{q}_1 - AC)]^2), \end{aligned} \quad (67)$$

in which is $\boldsymbol{\lambda}$ the costate vector. The optimality is given by the maximum principle [52]

$$\mathcal{H}(\mathbf{x}^*(t), u^*(t), \boldsymbol{\lambda}^*(t)) \le \mathcal{H}(\mathbf{x}^*(t), u(t), \boldsymbol{\lambda}^*(t)), \quad (68)$$

where the star represents the optimal trajectory and corresponding control and costate. On the optimal trajectory, all constraints are not violated. Then (68) can be rewritten as

$$\begin{aligned} & \mathcal{H}(\mathbf{x}^*(t), u^*(t), \boldsymbol{\lambda}^*(t)) = 1 + \lambda_1^* x_2^* + \lambda_2^* x_3^* + \lambda_3^* u^* \\ & \le \mathcal{H}(\mathbf{x}^*(t), u(t), \boldsymbol{\lambda}^*(t)) = 1 + \lambda_1^* x_2^* + \lambda_2^* x_3^* + \lambda_3^* u. \end{aligned} \quad (69)$$

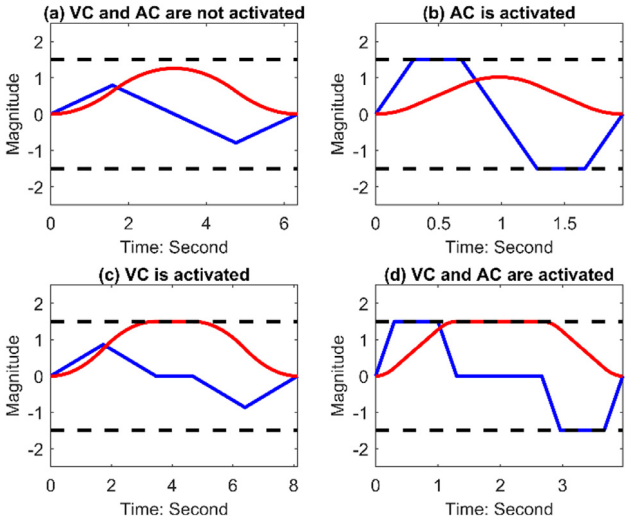

Fig. 10. Four canonical profiles for constraints (blue: acceleration, red: velocity, dash: AC and VC (they are equal in this example)).

Furthermore, we have

$$\lambda_3^* u^* \le \lambda_3^* u. \quad (70)$$

The optimal control u^* can be determined by the costate $\lambda_3^*(t)$

$$u^*(\mathrm{t}) = \begin{cases} JC, \lambda_3^* < 0 \\ \text{undetermined}, \ \lambda_3^* = 0 \\ -JC, \lambda_3^* > 0 \end{cases}. \quad (71)$$

It is obvious that control law (71) is a bang–bang control. However, (71) only describes the relationship between costate and input. In practice, the costate vector $\boldsymbol{\lambda}$ is difficult to solve due to constraints. Therefore, the switching time for bang–bang control must be calculated in other ways.

Instead of solving the costate vector, we use integral with corresponding boundary conditions to determine the input (bang–bang switching time).

The most challenge thing is to determine the boundary conditions. We know that there are three constraints including two state constraints and one input constraint. The input constraint is always activated due to the bang–bang control law. Each state constraint may be activated or not activated during the task, and there are four canonical profiles in total: VC and AC are not activated; AC is activated and VC is not activated; VC is activated and AC is not activated; VC and AC are activated; Fig. 10 illustrates four canonical profiles. For a given desired position q_d, JC, AC and VC, the first thing is to determine which canonical profile it is and then the solution can be solved by integral with corresponding boundary conditions.

For each canonical profile, the switching times can be solved by the initial and terminal conditions. The necessary conditions for each situation can be derived from the corresponding boundary conditions. Here, necessary conditions for the four canonical profiles are given.

For the first canonical profile, VC and AC are not activated. There are two switching times for this situation, and they are symmetric to $t = T/2$. The boundary conditions for this situation is

$$\begin{aligned} & q_1(0) = \dot{q}_1(0) = \ddot{q}_1(0) = 0, \\ & q_1(T/2) = q_d/2, \\ & \dddot{q}_1(T/2) = 0. \end{aligned} \quad (72)$$

And the necessary conditions are

$$\begin{aligned}&\dot{q}_1(T/2) < VC,\\&\ddot{q}_1(\tau_1) < AC,\end{aligned} \tag{73}$$

in which t_1 is the switching time of the jerk $\dddot{q}_1$. T and t_1 can be solved from the boundary conditions (72) and initial and terminal conditions in (63). In this case, $t_1 = (\frac{q_d}{2JC})^{1/3}$ and $T = 4t_1$. Rewrite (73) with q_d, JC, AC, VC, T and t_1, one can obtain

$$\begin{cases}JC(\frac{q_d}{2JC})^{\frac{2}{3}} < VC\\JC(\frac{q_d}{2JC})^{\frac{1}{3}} < AC\end{cases}. \tag{74}$$

Similarly, for only AC is activated, there are four switching times, and the corresponding boundary conditions are

$$\begin{aligned}&q_1(0) = \dot{q}_1(0) = \ddot{q}_1(0) = 0,\\&\ddot{q}_1(t_1) = \ddot{q}_1(t_2) = AC,\\&q_1(T/2) = q_d/2,\\&\ddot{q}_1(T/2) = 0.\end{aligned} \tag{75}$$

The switching times t_1, t_2 and T in this case are

$$t_1 = \frac{AC}{JC}, t_2 = \frac{\sqrt{AC\left(AC^3 + 4q_dJC^2\right)} - AC^2}{2ACJC}, T = 2(t_1 + t_2). \tag{76}$$

The corresponding necessary conditions are

$$\begin{aligned}&\dot{q}_1(T/2) < VC,\\&0 < t_1 < t_2 < T/2.\end{aligned} \tag{77}$$

Substituting (76) into (77) and we have

$$\begin{cases}\frac{VC\left(AC^2 + JCVC\right)}{ACJC} > q_d\\JC(\frac{q_d}{2JC})^{\frac{1}{3}} > AC\end{cases}. \tag{78}$$

For only VC is activated, we have four switching times and corresponding boundary conditions are

$$\begin{aligned}&q_1(0) = \dot{q}_1(0) = \ddot{q}_1(0) = 0,\\&q_1(T/2) = q_d/2,\\&\dot{q}_1(T/2) = VC,\\&\ddot{q}_1(T/2) = 0.\end{aligned} \tag{79}$$

In this case, the switching times and T are

$$\begin{aligned}&t_1 = \sqrt{VC/JC}, t_2 = 2t_1,\\&T = \frac{q_d}{VC} + t_2.\end{aligned} \tag{80}$$

Necessary conditions are

$$\begin{aligned}&\ddot{q}_1(t_1) < AC,\\&0 < t_1 < t_2 < T/2.\end{aligned} \tag{81}$$

Rewrite (81) and we can obtain

$$\begin{cases}\sqrt{VCJC} < AC\\JC(\frac{q_d}{2JC})^{\frac{2}{3}} > VC\end{cases}. \tag{82}$$

For the case that VC and AC are activated, there are six switching times in total and boundary conditions are

$$\begin{aligned}&q_1(0) = \dot{q}_1(0) = \ddot{q}_1(0) = 0,\\&\dot{q}_1(t_3) = \dot{q}_1(T/2) = VC,\\&\ddot{q}_1(t_1) = \ddot{q}_1(t_2) = AC,\\&q_1(T/2) = q_d/2,\\&\ddot{q}_1(T/2) = 0.\end{aligned} \tag{83}$$

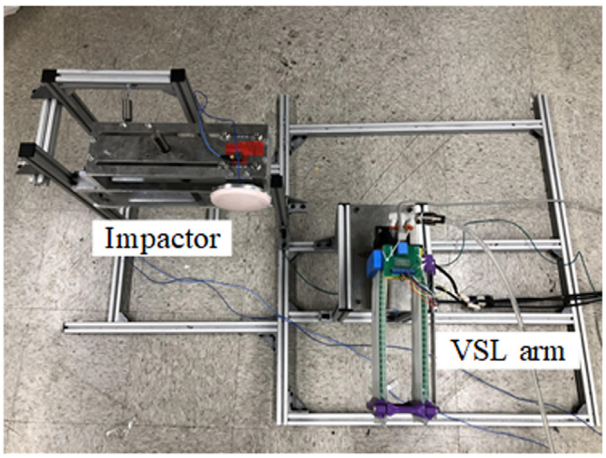

Fig. 11. VSL robot test bed.

In this case, the switching times and T are

$$\begin{aligned}&t_1 = AC/JC, t_2 = VC/AC, t_3 = t_1 + t_2,\\&T = 2t_3 + \frac{q_d}{VC} - \frac{t_2AC(AC + JCt_2)}{JCVC}.\end{aligned} \tag{84}$$

Necessary conditions are

$$0 < t_1 < t_2 < t_3 < T/2. \tag{85}$$

And it can be rewritten as

$$\begin{cases}\frac{VC\left(AC^2 + JCVC\right)}{ACJC} < q_d\\\sqrt{VCJC} > AC\end{cases}. \tag{86}$$

For any given constraints and desired position, the canonical profile can be determined from the necessary conditions (74), (78), (82) and (86). After that, the analytical solution of the optimal trajectory can be obtained from integral with corresponding boundary conditions. In practice, those solutions can be solved offline and be used in real-time applications.

The planning problem considers kinematic constraints and works for the rest-to-rest task. For arbitrary initial conditions, the derivations are more complicated than the rest-to-rest trajectory and we will not discuss it in this paper.

4. Experiments

In this section, experimental results of both motion test and impact test are presented.

4.1. Experimental setup

The test bed consists of a single-link VSL arm and a dummy head. Fig. 11 illustrates the test bed. Multiple sensors are installed on the arm and the dummy head to acquire data. On the dummy head, we set up an accelerometer and a force sensor on it to evaluate the impact. On the VSL arm, strain gauges are deployed to obtain deflection feedback. A pressure transducer is installed as well. More details are shown in Fig. 12.

The dummy head is made of aluminum and it is covered by silicone gel to mimic the material properties of human skin. A spring is added to mimic the stiffness of the human neck.

The core component of the electronic part is the National Instrument CompactRIO 9035 (CRIO) controller. The main task of the CRIO controller is the control task and data acquisition. The data acquisition cards on CRIO are NI 9411 (read encoder

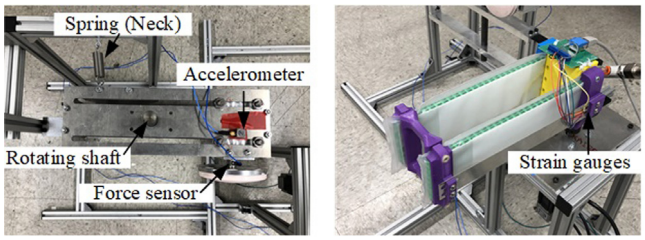

Fig. 12. Dummy head and VSL arm.

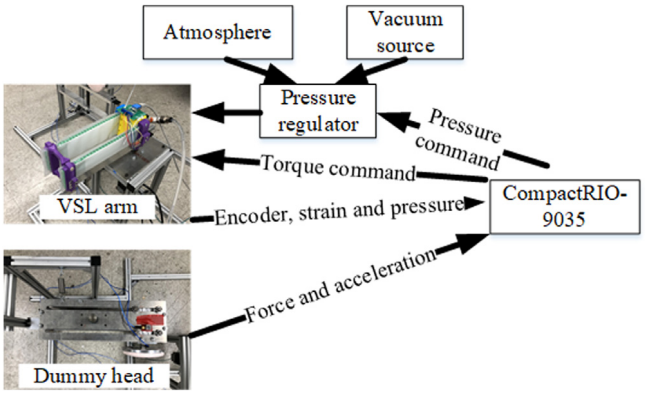

Fig. 13. System diagram of the test bed.

signal), NI 9237 (read strain gauge signal, sampling rate: 50 kS/s), NI 9222 (read force, acceleration and pressure, sampling rate: 20 kS/s), NI 9401 (PWM signal to pressure regulator), NI 9263 (torque command to the motor). The cycle time of the controller is 0.5 ms (2000 Hz), which should be fast enough to suppress the vibrations with low frequency. The natural frequency of the link can be roughly estimated by the link stiffness and the payload mass, which is $\omega = \sqrt{K_L/m_p}$. In this experiment, the natural frequency of the softest link configuration is 6.65 Hz. Fig. 13 shows the system diagram of the test bed. Table 1 shows the parameters of the experimental setup.

Table 1
Experimental setup.

Parameters	Value
Motor inertia (kg m^2)	0.00227
Dummy head Mass (kg)	2.5
Neck stiffness (N m/rad)	10
Link mass (kg)	0.2 each
Stiffness range (N/m)	140∼3900
Flexible link length (m)	0.22
Total length (m)	0.31
Payload mass (kg)	0.08

4.2. Motion test

In the motion test, a trajectory for a rest-to-rest task is planned. Constraints and desired position are selected as

$$\begin{cases} q_d = 180^\circ, \\ VC = 1\,\text{rad/s}, \\ AC = 1\,\text{rad/s}^2, \\ JC = 1\,\text{rad/s}^3. \end{cases} \tag{87}$$

In (87), AC is selected to fulfill the limits of stiffness actuator (response time). VC can be selected by (62) in practice. In this experiment, we directly choose $VC = 1\,\text{rad/s}$ for convenience.

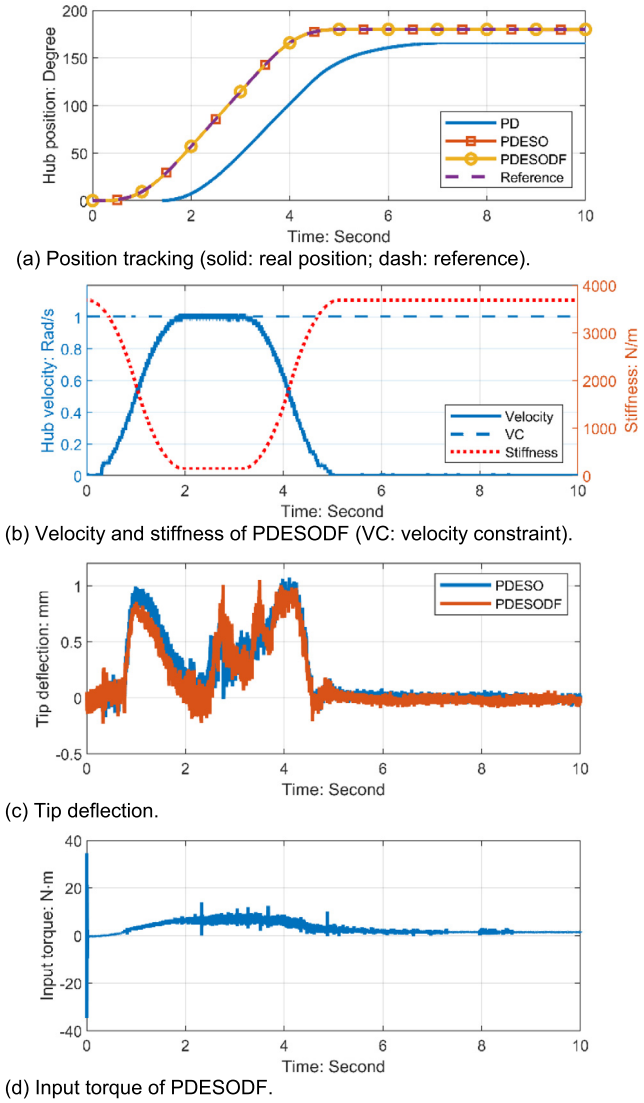

Fig. 14. Motion test results.

JC is selected to activate the VC. In engineering practice, a small JC value can also attenuate the vibration. During the motion, the stiffness is changing with the velocity

$$K = \frac{\dot{q}_d(K_{\min} - K_{\max})}{VC} + K_{\max}. \tag{88}$$

This linear relationship keeps the inherent safety of the VSL robot. When the robot moves fast, the arm transforms to soft setup to keep safe. When the robot moves slowly, the robot has better positioning performance and smaller vibration due to the large stiffness.

The parameters of the PD controller are $K_P = 25, K_D = 10$ and gains of the extended state observer are selected as $L = [3000 \quad 3000000 \quad 2000000000]$. The parameters of the deflection feedback are chosen as $\alpha_1 = 0.5, \alpha_2 = 8$. To make a comparison, different controller designs including the traditional feedback linearization PD controller (PD), PD controller with ESO (PDESO) and PDESO controller with deflection feedback (PDESODF) are used in the experiment. The parameters of the three controllers are the same. Fig. 14 shows the experimental results.

From Fig. 14. (a), the tracking of the desired hub angle trajectory is successful with PDESO and PDESODF. Without the ESO, the PD controller cannot handle uncertainties and disturbances.

Therefore, a large tracking error can be observed. From Fig. 14. (b), the velocity constraint is not violated during the task. Note the stiffness is also changed with the velocity to achieve safety in high speed and better positioning at low speed. The tip deflection is shown in Fig. 14. (c). The vibration of in the case of the PD controller is not shown in Fig. 14. (c) because it fails to track the desired hub angle. To evaluate the vibration, the root mean squares (RMS) of the tip deflection is introduced.

$$\psi = \sqrt{\frac{1}{t_2 - t_1}\int_{t_1}^{t_2} \delta_t^2(t)dt} \tag{89}$$

Both PDESO and PDESODF controller have small tip deflections. The RMS tip deflection of the PDESO is $\psi_{PDESO} = 0.45$ mm, while the PDESODF has a weaker vibration with $\psi_{PDESODF} = 0.41$ mm. The vibration in this test is suppressed very well. It is worth mentioning that the vibration suppression needs collaboration among the controller, jerk-limited trajectory, and mechanical design of the link. Fig. 14. (d) shows the input torque. From the experimental results above, the tracking control design for VSL robots is successful. Tracking performance and vibration suppression are achieved simultaneously.

4.3. Impact test

Besides the motion test, impact test is done to show the potential of VSL robots in human–robot interaction. As a comparison, the prototype is also tested in a stiff setup (constant stiffness link (CSL)). We compared the performance of CSL and the VSL under different velocity and contact stiffness (with or without soft covering material). A threshold for impact force $F_{thre} = 5$ N is set for the impact test. When the impact force is greater than the threshold, the motor torque input will be cut off. During the impact, acceleration of the dummy head and impact force are measured to evaluate the impact.

Figs. 15 and 16 show the results of the rigid impact (without covering materials). The rigid impact can be divided into two phases. The first phase starts from the beginning and it has a duration about four milliseconds in this test. The second phase starts around 3.675 s and it lasts much longer than the first phase. The first phase also has larger accelerations and force than the second phase. Between the two phases, the impact force is almost zero which means the robot and human have no impact between the two phases. In [11], similar two-phase impact test results are reported based on a prototype with a variable stiffness actuator.

It is obvious that VSL robot causes smaller force and acceleration than the CSL robot during the second phase. It means that the VSL robot is safer during the second phase. Fig. 16 shows the results of HIC in the first phase (without covering materials). From Fig. 16, the HIC generated by the VSL is smaller than the HIC generated by CSL. However, the reductions of force and acceleration caused by the VSL are not significant enough in the first phase. We can conclude that during the rigid impact (without covering materials), the VSL is safer than the CSL in the second phase. The severity of the first phase cannot be significantly reduced by using the VSL. The rigid impact usually has a large contact stiffness which makes the contact time of the first phase very short (4 ms in this test). The VSL cannot generate enough deflection to absorb the energy of the impact in such a short contact. Therefore, the VSL behaves almost the same as CSL in the first phase.

As a comparison, we add a foam pad as the covering materials of the robot. Figs. 17 and 18 show the results of soft impact test (with covering materials).

As can be seen from Fig. 17, the soft impact has only one phase. The contact time is much longer than the rigid impact. With enough contact time, the VSL can absorb the energy of the impact. Therefore, we can observe significant reductions on impact force and the acceleration of the dummy head.

Fig. 18 shows the HIC of the soft impact. Compared with the results in the rigid impact, the VSL can reduce the HIC significantly during the soft impact. Scenarios with velocity slower than

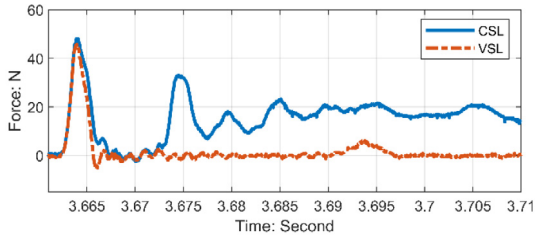

(a) Impact force.

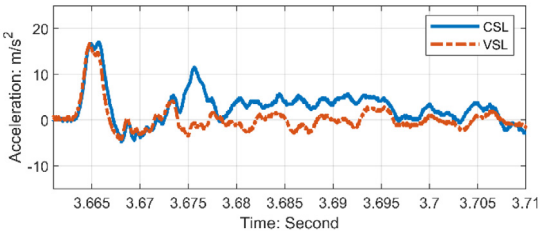

(b) Acceleration of the dummy head.

Fig. 15. Impact test results (VC = 1 rad/s (0.31 m/s, without covering materials)).

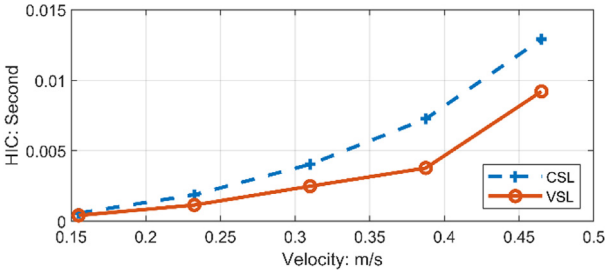

Fig. 16. HIC of the first phase. (Without covering materials.)

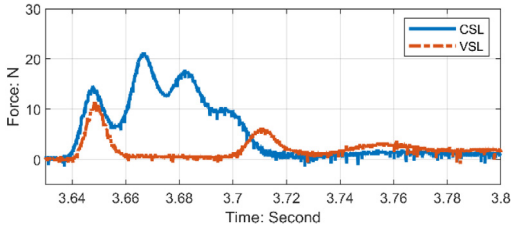

(a) Impact force.

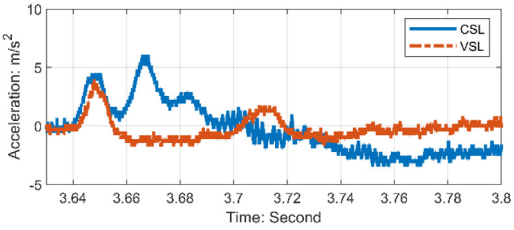

(b) Acceleration of the dummy head.

Fig. 17. Impact test results (VC = 1 rad/s (0.31 m/s, with covering materials)).

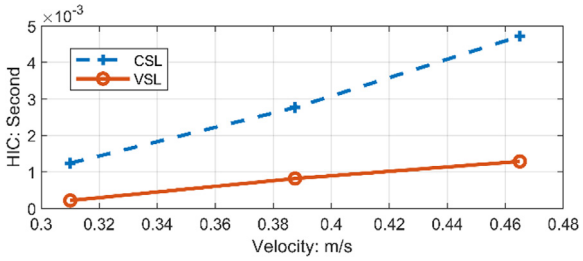

Fig. 18. HIC of the soft impact (with covering materials).

0.3 m/s are not tested in the soft impact test because the impact is too weak to trigger the force threshold.

5. Conclusions

In this paper, modeling, control design and trajectory planning for a single-link VSL robot are introduced. Dynamic modeling of the parallel-guided VSL is developed by the pseudo-rigid-body model. After that, the motion controller is designed based on the model and feedback linearization. The extended state observer and the deflection feedback are implemented to address the robustness and vibration suppression. In the trajectory planning problem, the safety criterion is converted to a velocity constraint. Besides velocity, jerk and acceleration constraints are considered to make the trajectory smooth, which can attenuate the potential vibrations during the motion. The analytical solution of the trajectory planning problem is given by the optimal control theory. Motion test shows that the controller achieves trajectory tracking and vibration suppression successfully. In the impact test, VSL shows better performance on safety for both rigid impact and soft impact. HIC and impact force can be reduced by the VSL. The proposed control and planning designs for VSL achieve the tracking and inherent safety simultaneously.

Declaration of competing interest

The authors declare that they have no known competing financial interests or personal relationships that could have appeared to influence the work reported in this paper.

References

[1] S. Haddadin, A. Albu-Schaffer, A.D. Luca, G. Hirzinger, Collision detection and reaction: A contribution to safe physical human-robot interaction, in: 2008 IEEE/RSJ International Conference on Intelligent Robots and Systems, Nice, France, 2008.
[2] A. Stilli, L. Grattarola, H. Feldmann, H.A. Wurdemann, K. Althoefer, Variable stiffness link (VSL): Toward inherently safe robotic manipulators, in: 2017 IEEE International Conference on Robotics and Automation (ICRA), Singapore, Singapore, 2017.
[3] S. Haddadin, A.D. Luca, A. Albu-Schäffer, Robot collisions: A survey on detection, isolation, and identification, IEEE Trans. Robot. 33 (6) (2017) 1292–1312.
[4] S. Haddadin, A. Albu-Schaffe, G. Hirzinger, Safety evaluation of physical human-robot interaction via crash-testing, in: Robotics: Science and Systems Conference 2007 (RSS2007), Atlanta, USA, 2007.
[5] F. Flacco, T. Kroger, A.D. Luca, O. Khatib, A depth space approach to human-robot collision avoidance, in: 2012 IEEE International Conference on Robotics and Automation, Saint Paul, USA, 2012.
[6] E.A. Sisbot, R. Alami, A human-aware manipulation planner, IEEE Trans. Robot. 28 (5) (2012) 1045–1057.
[7] Y. She, H.-J. Su, D. Meng, S. Song, J. Wang, Design and modeling of a compliant link for inherently safe corobots, J. Mech. Robot. 10 (1) (2018) JMR–17–1087.
[8] S.-D. Lee, B.-S. Kim, J.-B. Song, Human–robot collision model with effective mass and manipulability for design of a spatial manipulator, Adv. Robot. 27 (3) (2013) 189–198.
[9] G. Tonietti, R. Schiavi, A. Bicchi, Design and control of a variable stiffness actuator for safe and fast physical human/robot interaction, in: Proceedings of the 2005 IEEE International Conference on Robotics and Automation, Barcelona, Spain, 2005.
[10] R. Qi, A. Khajepour, W.W. Melek, T.L. Lam, Y. Xu, Design, kinematics, and control of a multijoint soft inflatable arm for human-safe interaction, IEEE Trans. Robot. 33 (3) (2017) 594–609.
[11] R. Schiavi, G. Grioli, S. Sen, A. Bicchi, VSA-II: a novel prototype of variable stiffness actuator for safe and, in: 2008 IEEE International Conference on Robotics and Automation, Pasadena, USA, 2008.
[12] Y. She, Compliant Robotic Arms for Inherently Safe Physical Human–Robot Interaction, The Ohio State University, 2018.
[13] A. Jiang, G. Xynogalas, P. Dasgupta, K. Althoefer, T. Nanayakkara, Design of a variable stiffness flexible manipulator with composite granular jamming and membrane coupling, in: 2012 IEEE/RSJ International Conference on Intelligent Robots and Systems, Vilamoura, Portugal, 2012.
[14] A. Stilli, H.A. Wurdemann, a.K. Althoefer, A novel concept for safe, stiffness-controllable robot links, Soft Robot. 4 (1) (2017) 16–22.
[15] C. Hurd, Variable Stiffness Robotic Arm for Safe Human-Robot Interaction using Layer Jamming (Undergraduate Thesis), The Ohio State University, 2017.
[16] L. Hao, C. Xiang, M. Giannaccini, H. Cheng, S.N.-M. Ying Zhang, S. Davis, Design and control of a novel variable stiffness soft arm, Adv. Robot. 32 (11) (2018) 605–622.
[17] A. DeLuca, B. Siciliano, Trajectory control of a non-linear one-link flexible arm, Internat. J. Control 50 (5) (1989) 1699–1715.
[18] M. Vandegrift, F. Lewis, S. Zhu, Flexible-link robot arm control by a feedback linearization/singular perturbation approach, J. Robot. Syst. 11 (7) (1994) 591–603.
[19] W. Singhose, Command shaping for flexible systems: A review of the first 50 years, Int. J. Precis. Eng. Manuf. 10 (4) (2009) 153–168.
[20] R. Morales, V. Feliub, V. Jaramillo, Position control of very lightweight single-link flexible arms with large payload variations by using disturbance observers, Robot. Auton. Syst. 60 (4) (2012) 532–547.
[21] S.E. Talole, J.P. Kolhe, S.B. Phadke, Extended-state-observer-based control of flexible-joint system with experimental validation, IEEE Trans. Ind. Electron. 57 (4) (2010) 1411–1419.
[22] M. Giannaccini, C. Xiang, A. Atyabi, T. Theodoridis, S. Nefti-Meziani, S. Davis, Novel design of a soft lightweight pneumatic continuum robot arm with decoupled variable stiffness and positioning, Soft Robot. 5 (1) (2018) 54–70.
[23] P.W. Nan Lin, M. Wang, J. Wei, F. Yang, S. Xu, Z. Ye, X. Chen, IMU-based active safe control of a variable stiffness soft actuator, IEEE Robot. Autom. Lett. 4 (2) (2019) 1247–1254.
[24] Y.-Q. Yu, L.L. Howell, C. Lusk, Y. Yue, M.-G. He, Dynamic modeling of compliant mechanisms based on the pseudo-rigid-body model, J. Mech. Des. 127 (4) (2005) 760–765.
[25] Y. She, D. Meng, H.-J. Su, S. Song, J. Wang, Introducing mass parameters to pseudo–rigid–body models for precisely predicting dynamics of compliant mechanisms, Mech. Mach. Theory 126 (2018) 273–294.
[26] J. Huang, P. Hu, K. Wu, M. Zeng, Optimal time-jerk trajectory planning for industrial robots, Mech. Mach. Theory 121 (2017) 530–544.
[27] A. Gasparetto, V. Zanotto, A technique for time-jerk optimal planning of robot trajectories, Robot. Comput.-Integr. Manuf. 24 (3) (2008) 415–426.
[28] A. Gasparetto, V. Zanotto, Optimal trajectory planning for industrial robots, Adv. Eng. Softw. 41 (4) (2010) 548–556.
[29] M.M.G. Ardakani, B. Olofsson, A. Robertsson, R. Johansson, Model predictive control for real-time point-to-point trajectory generation, IEEE Trans. Autom. Sci. Eng. Early access (2018) 1–12.
[30] A. Shafei, M. Korayem, Theoretical and experimental study of DLCC for flexible robotic arms in point-to-point motion, Optim. Control Appl. Methods 38 (6) (2017) 963–972.
[31] A. Bicchi, G. Tonietti, Fast and soft-arm tactics, IEEE Robot. Autom. Mag. 11 (2) (2004) 22–33.
[32] R. Haschke, E. Weitnauer, H. Ritter, On-line planning of time-optimal, jerk-limited trajectories, in: 2008 IEEE/RSJ International Conference on Intelligent Robots and Systems, Nice, France, 2008.
[33] T. Kroger, Online trajectory generation: Straight-line trajectories, IEEE Trans. Robot. 27 (5) (2011) 1010–1016.
[34] Y. Wei, Y. Chen, T. Ren, Q. Chen, C. Yan, Y. Yang, Y. Li, A. Novel, Variable stiffness robotic gripper based on integrated soft actuating and particle jamming, Soft Robot. 3 (3) (2016) 134–143.
[35] S. Hauser, M. Robertson, A. Ijspeert, J. Paik, Jammjoint: A variable stiffness device based on granular jamming for wearable joint support, IEEE Robot. Autom. Lett. 2 (2) (2017) 849–855.
[36] E. Brown, N. Rodenberg, J. Amend, A. Mozeika, E. Steltz, M.R. Zakin, H. Lipson, H.M. Jaeger, Universal robotic gripper based on the jamming of granular material, Proc. Natl. Acad. Sci. 107 (44) (2010) 18809–18814.

[37] Y. She, H.-J. Su, Cheng Lai, D. Meng, Design and prototype of a tunable stiffness arm for safe human–robot interaction, in: ASME 2016 International Design Engineering Technical Conferences and Computers and Information in Engineering Conferenc, Charlotte, NC, USA, 2016.
[38] L.L. Howell, A. Midha, Parametric deflection approximations for end-loaded, large-deflection beams in compliant mechanisms, J. Mech. Des. 117 (1) (1995) 156–165.
[39] H.-J. Su, A pseudorigid-body 3R model for determining large deflection of cantilever beams subject to tip loads, J. Mech. Robot. 1 (2) (2009) 021008–021009.
[40] V.K. Venkiteswaran, H.-J. Su, A three-spring pseudorigid-body model for soft joints with significant elongation effects, J. Mech. Robot. 8 (6) (2016) 061001–061007.
[41] Y.-Q. Yu, L.L. Howell, C. Lusk, Y. Yue, M.-G. He, Dynamic modeling of compliant mechanisms based on the pseudo-rigid-body model, J. Mech. Des. 127 (4) (2005) 760–765.
[42] Y. She, D. Meng, S. Song, J. Wang, H.-J. Su, Introducing mass parameters to pseudo-rigid-body models for precisely predicting dynamics of compliant mechanisms, Mech. Mach. Theory 126 (2018) 273–294.
[43] J. Derderian, L. Howell, M. Murphy, S. Lyon, S. Pack, Compliant parallel-guiding mechanisms, in: Proceedings of the 1996 ASME Mechanisms Conference, 1996.
[44] M. Spong, M. Vidyasagar, Robot Dynamics and Control, John Wiley & Sons, 1989.
[45] M. Korayem, A. Shafei, M. Doosthoseini, F. Absalan, B. Kadkhodaei, Theoretical and experimental investigation of viscoelastic serial robotic manipulators with motors at the joints using timoshenko beam theory and gibbs–appell formulation, Proc. Inst. Mech. Eng. K 230 (1) (2016) 37–51.
[46] H.K. Khalil, Noninear Systems, Prentice-Hall, New Jersey, 1996.
[47] Q. Zheng, L.Q. Gao, Z. Gao, On validation of extended state observer through analysis and experimentation, J. Dyn. Syst. Meas. Control 134 (2) (2012).
[48] D. Gao, C.W. Wampler, Head injury criterion, IEEE Robot. Autom. Mag. 16 (4) (2009) 71–74.
[49] S. Haddadin, Sami Haddadin, Towards Safe Robots: Approaching Asimov's 1st Law, Springer, 2013.
[50] J. Echávarri, M. Ceccarelli, G. Carbone, C. Alén, J.L. Muñoz, A. Díaz, J.M. Munoz-Guijosa, Towards a safety index for assessing head injury potential in service robotics, Adv. Robot. 27 (11) (2013) 831–844.
[51] S. Haddadin, A. Albu-Schäffer, G. Hirzinger, The role of the robot mass and velocity in physical human-robot interaction - part I: Non-constrained blunt impacts, in: IEEE International Conference on Robotics and Automation, Pasadena, USA, 2008.
[52] D. Kirk, Optimal Control Theory: An Introduction, Courier Corporation, 2012.

Siyang Song received the B.S. degree and M.S. degree in control engineering from Beihang University, Beijing, China, in 2013 and 2016, respectively. He is now a Ph.D. student in the University of Texas at Austin. His research interests include dynamics, modeling and control for flexible systems, physical human–robot interaction and human–robot collaboration.

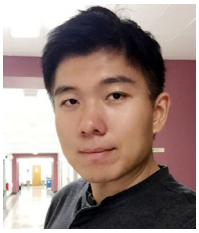

Xianpai Zeng received the B.S. degree in mechanical engineering from The Ohio State University, Columbus, OH, USA, in 2015; and M.S. degree from the University of California, Los Angeles, CA, USA, in 2016. He is now a Ph.D. student in The Ohio State University. His research interests include design and FEM simulation, compliant mechanisms, variable stiffness robotic arms, soft robots, and physical human–robot interaction (pHRI).

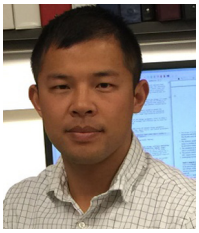

Yu She received his bachelor's degree in Mechanical Engineering at Taiyuan University of Technology, Taiyuan, China (2011). He obtained his Master's degree in Mechanical and Automation at Harbin Institute of Technology, Shenzhen, China (2014). He obtained his Ph.D. degree in Mechanical Engineering at The Ohio State University (2018). He currently works as a postdoctoral associate in Computer Science & Artificial Intelligence Laboratory at Massachusetts Institute of Technology. His research interests include Design, Compliant mechanisms, Mechatronics, Mobile robots, Soft robots, and Physical Human–Robot Interaction.

Junmin Wang received the B.E. degree in automotive engineering and the M.S. degree in power machinery and engineering from Tsinghua University, Beijing, China, in 1997 and 2000, respectively; the second and third M.S. degrees in electrical engineering and mechanical engineering from the University of Minnesota, Twin Cities, Minneapolis, MN, USA, in 2003; and the Ph.D. degree in mechanical engineering from the University of Texas at Austin, Austin, TX, USA, in 2007. Dr. Wang is the Accenture Endowed Professor in Department of Mechanical Engineering at University of Texas at Austin. His major research interests include control, modeling, estimation, and diagnosis of dynamical and mechatronic systems. Prof. Wang is an IEEE Vehicular Technology Society Distinguished Lecturer (2015–2019), SAE Fellow (2015), and ASME Fellow (2016).

Hai-Jun Su received the Ph.D. degree in mechanical engineering from the University of California, Irvine, CA, USA, in 2004. He is an Associate Professor with the Department of Mechanical and Aerospace Engineering, The Ohio State University (OSU), Columbus, OH, USA. Prior to joining OSU in September 2011, he was an Assistant Professor of mechanical engineering at the University of Maryland, Baltimore County (2007–2011) and a Postdoctoral Associate with the Virtual Reality Application Center, Iowa State University (2004–2007). Dr. Su received the MSC Software Simulation Paper Award in 2002, was a finalist for the Mechanism and Robotics Best Paper Award in 2005, and received the NSF Faculty Early Career Development (CAREER) Award in 2008, the Compliant Mechanism Theory Best Paper Award in 2009 and 2014, the Air Force Summer Faculty Fellowship and ASME M&R Freudenstein/GM Young Investigator Award in 2010, and the Lumley Research Award in 2015. He is an Associate Editor of the ASME Journal of Mechanisms and Robotics and served as the Chair of the 2016 ASME Mechanisms and Robotics Conference. He is a Fellow of ASME (2017).